Regular Article

A circle swimmer at low Reynolds number

R. Ledesma-Aguilar[1,a], H. Löwen[2], and J.M. Yeomans[1]

[1] The Rudolf Peierls Centre for Theoretical Physics, University of Oxford, 1 Keble Road, Oxford OX1 3NP, UK
[2] Institut für Theoretische Physik II: Weiche Materie, Heinrich-Heine-Universität Düsseldorf, Universitätsstraße 1, D-40225 Düsseldorf, Germany

Abstract. Swimming in circles occurs in a variety of situations at low Reynolds number. Here we propose a simple model for a swimmer that undergoes circular motion, generalising the model of a linear swimmer proposed by Najafi and Golestanian (Phys. Rev. E **69**, 062901 (2004)). Our model consists of three solid spheres arranged in a triangular configuration, joined by two links of time-dependent length. For small strokes, we discuss the motion of the swimmer as a function of the separation angle between its links. We find that swimmers describe either clockwise or anticlockwise circular motion depending on the tilting angle in a non-trivial manner. The symmetry of the swimmer leads to a quadrupolar decay of the far flow field. We discuss the potential extensions and experimental realisation of our model.

1 Introduction

The physics of microswimmers is a rapidly advancing field, for recent reviews see [1–4]. One of the simplest models of a microswimmer was proposed by Najafi and Golestanian [5] in 2004: it consists of three aligned spheres that are linked by rigid rods whose lengths change in time between two values. Moving with a periodic motion which breaks the time-reversal symmetry, this simple swimmer experiences a net propulsion along the rod orientation. A number of other swimmer models have been proposed subsequently [6–14], most of which lead to propulsion along a linear trajectory.

However, there are many examples in nature showing circle swimming rather than swimming along a straight line. On a planar substrate, certain bacteria [15–20] and spermatozoa [21–23] swim in circles. Moreover, spherical camphors have been shown to exhibit circular swimming when confined to an interface [24]. Recently, catalytically or thermally driven colloidal particles with an asymmetric shape have been prepared [25] also resulting in circular motion on a substrate [26].

Even though circle swimming is frequent in the presence of solid surfaces, curved trajectories are also very common in the bulk [27]. This can be attributed to asymmetries in the swimming stroke that can result in both translational and rotational modes of motion [28]. Therefore, while linear swimming occurs for highly symmetric swimmers, more generally swimming can occur along curved or circular trajectories.

The modelling of circle swimmers is much less advanced than that of their linearly moving counterparts. For instance, Dunstan *et al.* [29] considered a swimmer model of two spheres with different radii, which is a linear swimmer in a bulk fluid but yields circle swimming close to a solid surface. Shum *et al.* [30] have implemented a detailed model of a flagellate that exhibits circle swimming at surfaces. For circle swimmers in the bulk, minimal rotor models [7,8,31,32] or very coarse-grained driven Brownian particle models [33–35] have been proposed. For the latter, the particles proceed with both an effective translational and angular propagation velocity and experience additional Brownian fluctuations. The deterministic (noise-free) trajectory in two dimensions is a closed circle. However, a more detailed model which resolves the hydrodynamic details of the swimming strokes is missing.

In this paper we close this gap and generalise the linear model of Najafi and Golestanian [5] to a simple circle swimmer. In order to do so, we consider three spheres joined by two links which are tilted relative to each other and perform the stroke as in the Najafi-Golestanian model. By using both analytical and numerical methods, we show that the resulting motion is a closed circle which depends on the swimmer angle, β, which characterises the separation between the links. We focus on the resulting radius of the trajectories, R_t, as a function of β for strokes of small amplitude. Interestingly, we find that swimming occurs predominantly along one direction of the circular trajectory (anticlockwise for the specific configuration studied here), except for a small range of angles, where the swimmer reverses the sense of rotation. Such a behaviour is robust to changes in the model parameters. We
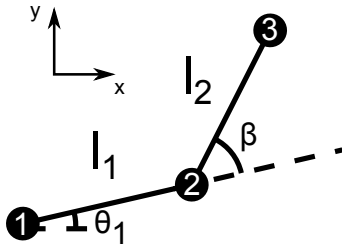
a e-mail: r.ledesmaaguilar1@physics.ox.ac.uk

Fig. 1. Model of a circle swimmer. Three spherical beads of identical radius R are joined by two links of variable length, l_1 and l_2. The angle between the links, $\beta \neq 0$, allows the swimmer to move in a curved trajectory.

further analyse the velocity field produced by this simple circle swimmer and find a marked inverse-power decay at large distances. We recover the expected quadrupolar far-field behaviour [8], with the magnitude of the velocity field decaying as the inverse cube of the distance from the swimmer. This is a consequence of the symmetry of the swimming stroke, which is invariant under combined time-reversal and parity transformations [36,37]. For asymmetric swimming strokes, which do not posses the time-reversal and parity symmetry, we recover a decay consistent with a dipolar velocity field, as expected.

Our simple model can serve as a starting point for further analytical and numerical studies. These can include single circle swimmers in confinement [33,34] and shear flow [38] as well as the scattering [37,39] and synchronization [40–42] of two circle swimmers and the (still unknown) collective properties of many circle swimmers, for example swarming and vortex formation.

The rest of the paper is organised as follows: in sect. 2, we describe and define the model. A discussion of the geometry of the resulting trajectory is performed in sect. 3 while the velocity fields in the surrounding fluid are discussed in sect. 4. Finally we conclude in sect. 5.

2 Model

Our model swimmer consists of three beads connected by two massless links, as depicted in fig. 1. These are separated by the swimmer angle, β, and have lengths, l_1 and l_2, which are known functions of time, and hence determine the swimming stroke.

The configuration of the swimmer can be characterised by the position vectors of the beads, $\mathbf{r}_i$, which are related by the conditions $\mathbf{r}_{12} = l_1 \hat{\mathbf{t}}_1$, and $\mathbf{r}_{23} = l_2 \hat{\mathbf{t}}_2$, where $\mathbf{r}_{ij} \equiv \mathbf{r}_j - \mathbf{r}_i$ and $\hat{\mathbf{t}}_i$ is the unit tangent vector to link l_i. Since, by symmetry, motion can only occur in the plane defined by $\hat{\mathbf{t}}_1$ and $\hat{\mathbf{t}}_2$, the orientation of the swimmer is determined by a single angle. Here we choose the polar angle associated with $\hat{\mathbf{t}}_1$, θ_1; the polar angle associated with $\hat{\mathbf{t}}_2$ hence obeys $\theta_2 = \theta_1 + \beta$. The swimming stroke imposes kinematic conditions for the bead velocity vectors, $\mathbf{v}_i \equiv \dot{\mathbf{r}}_i$, where the dot indicates differentiation with respect to time. For the tangential motion, corresponding to the contraction and extension of the links

$$(\mathbf{v}_2 - \mathbf{v}_1) \cdot \hat{\mathbf{t}}_1 = \dot{l}_1 \tag{1}$$

and

$$(\mathbf{v}_3 - \mathbf{v}_2) \cdot \hat{\mathbf{t}}_2 = \dot{l}_2, \tag{2}$$

while for the angular velocities

$$\frac{(\mathbf{v}_2 - \mathbf{v}_1) \cdot \hat{\boldsymbol{n}}_1}{l_1} - \frac{(\mathbf{v}_3 - \mathbf{v}_2) \cdot \hat{\boldsymbol{n}}_2}{l_2} = \dot{\beta}, \tag{3}$$

where $\dot{\hat{t}}_i = \dot{\theta}_i \hat{\boldsymbol{n}}_i$.

The bead dynamics in the overdamped limit is given by

$$\mathbf{v}_i = \sum_{j=1}^{3} \mathbf{H}_{ij} \cdot \mathbf{F}_j, \tag{4}$$

where the velocity of bead i results from the force acting on each bead, $\mathbf{F}_j$, mediated by the hydrodynamic interaction tensor, $\mathbf{H}_{ij}$, summed over all beads. For a Newtonian fluid of viscosity η, the hydrodynamic interactions can be described using the Oseen tensor

$$\mathbf{H}_{ij} = \begin{cases} \mathbb{1}/6\pi\eta R, & \text{if } i = j, \\ 1/8\pi\eta r_{ij} \left(\mathbb{1} + \mathbf{r}_{ij}\mathbf{r}_{ij}/r_{ij}^2 \right), & \text{if } i \neq j, \end{cases} \tag{5}$$

which is valid in the limit $R/r_{ij} \ll 1$.

To complete the model, we impose force-free and torque-free conditions on the swimmer

$$\sum_{i=1}^{3} \mathbf{F}_i = 0 \tag{6}$$

and

$$\sum_{i=1}^{3} \mathbf{r}_i \times \mathbf{F}_i = 0. \tag{7}$$

Equations (1)–(7) constitute a linear system for the bead velocities and forces, whose solution depends on time through $l_1(t)$, $l_2(t)$ and $\beta(t)$ —which are prescribed functions of time— and through $\theta_1(t)$, which reflects the dependence on the particular frame of reference and satisfies $\dot{\theta}_1 = (\mathbf{v}_2 - \mathbf{v}_1) \cdot \hat{\boldsymbol{n}}_1/l_1$. Once $\theta_1(t)$ is known, the evolution of the swimmer configuration and force distribution can be obtained by time integrating $\mathbf{v}_i$ and $\mathbf{F}_i$.

Following refs. [5] and [8] we consider a four-step swimming stroke, where the links contract and expand alternately at constant velocity W from an initial extension D with a change in length ϵ. This has the advantage of simplifying the analytics considerably, although other choices of the swimming stroke, consisting for instance in a continuous sinusoidal link variation, are also possible. The time evolution of the length of the links is chosen to be

$$l_1(t) = \begin{cases} D - Wt, & \text{if } 0 \leq t < P/4, \\ D - \epsilon, & \text{if } P/4 \leq t < P/2, \\ D - \epsilon + Wt, & \text{if } P/2 \leq t < 3P/4, \\ D, & \text{if } 3P/4 \leq t < P, \end{cases} \tag{8}$$
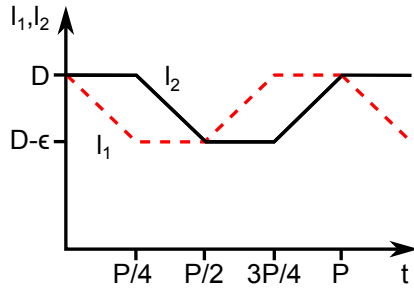
Fig. 2. Piece-wise swimming stroke. The links of the swimmer, of maximum extension D, contract and expand out of phase by a small length ϵ (exaggerated in the figure) over a period P.

and

$$
l_2(t) = \begin{cases} D, & \text{if } 0 \le t < P/4, \\ D - Wt, & \text{if } P/4 \le t < P/2, \\ D - \epsilon, & \text{if } P/2 \le t < 3P/4, \\ D - \epsilon + Wt, & \text{if } 3P/4 \le t < P, \end{cases} \tag{9}
$$

and is repeated subsequently over a period P. As shown in fig. 2, the swimming stroke dictated by eqs. (8) and (9) breaks the time-reversal symmetry, and thus results in a net propulsion of the swimmer.

3 Swimmer trajectories

We treat the problem analytically by first solving the linear system (1)–(7), we subsequently expand $\mathbf{v}_i$ in powers of R/D (up to first order), and ϵ/D and β (up to third order) and restrict ourselves to the case where β is constant in time. We are interested in the trajectory described by the swimmer, which can be characterised by angular and translational displacements over one period of the swimming stroke, $\Delta\theta$ and $\Delta\mathbf{r}$, respectively. Given that we expect only a small angular displacement within each step of the stroke cycle, it is sensible to shift to the frame of reference where $\theta_1(0) = 0$ at each step and perform an expansion in powers of θ_1. Keeping only the leading-order term in the expansion (constant angular velocity approximation) and adding the contribution of each step of the swimming stroke, we obtain, for the angular displacement,

$$
\Delta\theta \equiv \int_0^P \dot{\theta}_1 dt \approx \frac{5}{32}\left(\frac{R}{D}\right)\left(2\left(\frac{\epsilon}{D}\right)^2 + 3\left(\frac{\epsilon}{D}\right)^3\right)
$$
$$
\times \left(\beta - \frac{77}{180}\beta^3\right). \tag{10}
$$

For the translational displacement vector of the center of mass, $\Delta\mathbf{r} \equiv \int_0^P \frac{1}{3}\sum_{i=1}^3 \mathbf{v}_i dt = \Delta x \hat{\boldsymbol{e}}_{\boldsymbol{x}} + \Delta y \hat{\boldsymbol{e}}_{\boldsymbol{y}}$, we obtain

$$
\Delta x \approx R\left(\left(\frac{\epsilon}{D}\right)^2 + \left(\frac{\epsilon}{D}\right)^3\right)\left(\frac{7}{12} - \frac{53}{144}\beta^2\right)
$$
$$
- \frac{5R}{4608}\left(\frac{R}{D}\right)\left(2\left(\frac{\epsilon}{D}\right)^2 + 33\left(\frac{\epsilon}{D}\right)^3\right)\beta^2 \tag{11}
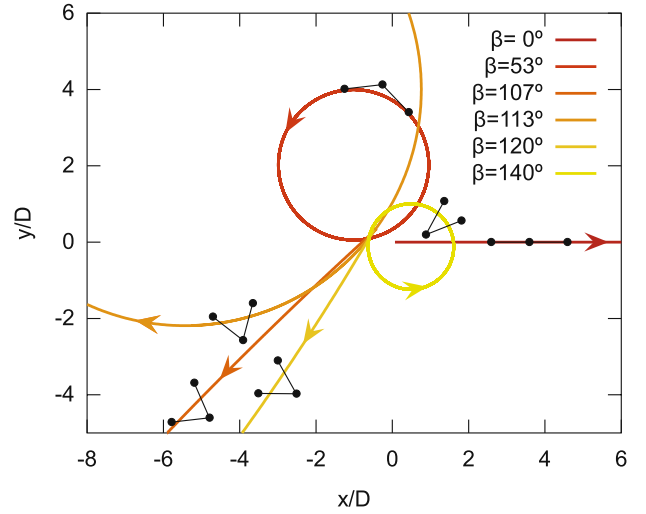$$

Fig. 3. Circular trajectories for swimmers at constant swimmer angle, β. Parameter values are $\epsilon/D = R/D = 10^{-1}$.

and

$$
\Delta y \approx R\left(\left(\frac{\epsilon}{D}\right)^2 + \left(\frac{\epsilon}{D}\right)^3\right)\left(\frac{7}{24}\beta - \frac{53}{144}\beta^3\right)
$$
$$
- \frac{5R}{9216}\left(\frac{R}{D}\right)\left(2\left(\frac{\epsilon}{D}\right)^2 + 33\left(\frac{\epsilon}{D}\right)^3\right)\beta^3. \tag{12}
$$

Equations (10)–(12) reduce to the result reported by Earl *et al.* [8] for vanishing β, where the swimmer moves along a linear trajectory with a displacement per swimming stroke

$$
\Delta\mathbf{r} \approx R\left(\frac{7}{12}\right)\left(\left(\frac{\epsilon}{D}\right)^2 + \left(\frac{\epsilon}{D}\right)^3\right)\hat{\boldsymbol{e}}_{\boldsymbol{x}}. \tag{13}
$$

For small, but finite, β the trajectory is no longer linear; according to eqs. (10)–(12) the swimmer undergoes a small positive rotation, and a translation along the x and y directions, thus describing a curved trajectory. While $\Delta\theta$ and Δy are odd functions of β, Δx is an even function of the swimmer angle; this is consistent with the symmetry of the trajectory under the transformation $\beta \to -\beta$, which corresponds to a reflection about the x-axis and has the effect reversing the sense of rotation and motion along the y-direction while keeping the translation along x unchanged.

Given that for a given β value $\Delta\theta$ and $|\Delta\mathbf{r}|$ are constants, the stroke-averaged trajectories form equilateral chains, becoming regular polygons whenever $\Delta\theta = 2\pi/m$ for integer m. Furthermore, due to the smallness of the angular displacement, the trajectories approach closed circles with curvature

$$
\frac{1}{R_t} \approx \frac{\Delta\theta}{|\Delta\mathbf{r}|} \approx \frac{15}{56}\left(2 + \left(\frac{\epsilon}{D}\right) - \left(\frac{\epsilon}{D}\right)^2 + \left(\frac{\epsilon}{D}\right)^3\right)\frac{\beta}{D}. \tag{14}
$$

In order to verify this assertion, and to explore the full range of β, we carry out numerical simulations for the motion of the swimmer, integrating the Oseen-level hydrodynamics over time. Numerical simulations are performed following the algorithm proposed in ref. [8]. At a
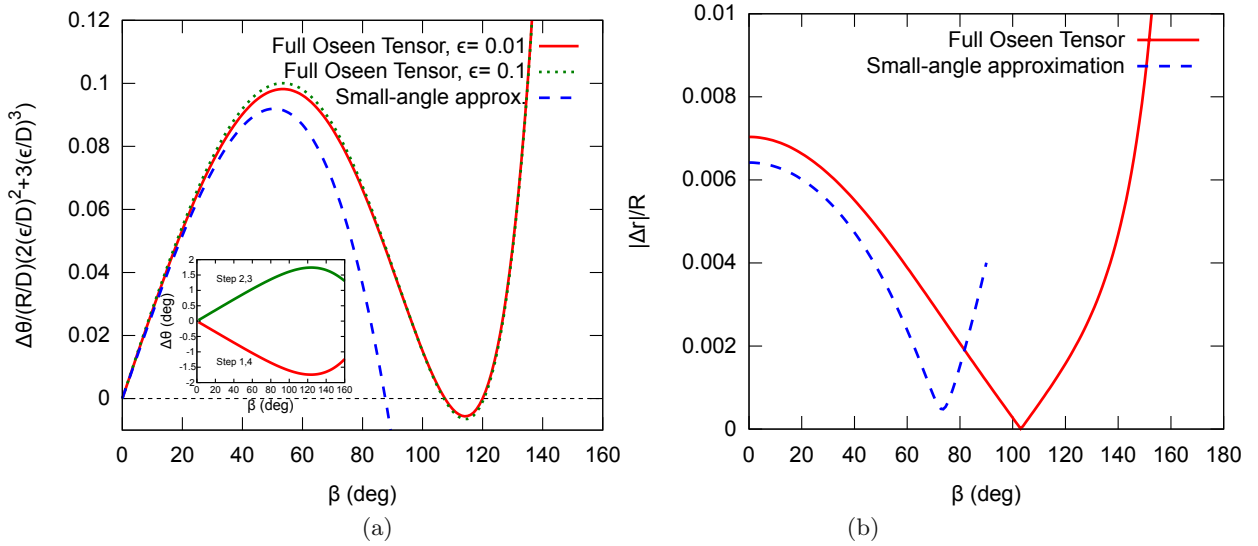
Fig. 4. (a) Normalised angular displacement as a function of the swimmer angle β. Numerical results for the full Oseen-tensor hydrodynamics are carried out for $\epsilon = 10^{-2}$ (solid line) and $\epsilon = 10^{-1}$ (dots). The dashed curve corresponds to the perturbative result. Inset: angular displacement during each step of the swimming stroke as a function of β. (b) Translational displacement as a function of β for $\epsilon = 10^{-1}$ (solid line). The dashed curve corresponds to the perturbative result.

given timestep, the swimmer shape is first updated according to the prescribed swimming stroke, while the position of its centre of mass and orientation are kept constant. We then use an iterative algorithm to find the position and orientation that satisfy the force-free and torque-free conditions. Swimmer trajectories, with the swimmer superimposed at an arbitrary time, are shown in fig. 3. As expected, trajectories are very close to circular. Figure 4 shows plots of $\Delta\theta$ and $|\Delta\mathbf{r}|$ as a function of β, where we also plot the perturbative result, given by eqs. (10)–(12). The angular displacement, depicted in fig. 4(a), shows a good agreement with the analytics up to angles as large as $\beta \approx 40°$. As suggested by eq. (10), results follow the same master curve for different deformations ($\epsilon/D = 10^{-1}$ and $\epsilon/D = 10^{-2}$) when rescaling by the amplitude $(R/D)(2(\epsilon/D)^2 + 3(\epsilon/D)^3)$. This indicates that the shape of the curve is a function of β only and, consequently, that the location of maxima and minima is independent of both R/D and ϵ/D. Figure 4(b) shows the magnitude of the translational displacement, which captures the main qualitative features of the numerical result. The slight discrepancy at small β can be attributed to corrections in R/D and ϵ/D as discussed in ref. [8] for linear swimmers.

While their trajectories are always circular, the sense of rotation of the swimmers changes depending on β, as shown in fig. 4(a). Such a dependence results from the competition between the four steps in the swimming stroke. During step 1, l_1 contracts and bead 3 moves to the left, experiencing a drag pointing to the right (see fig. 1). As a consequence, there is a torque acting on l_1 that causes a negative rotation of the swimmer. A similar reasoning can be used to conclude that the angular displacement must be positive for step 2. Step 3 can be mapped onto

step 2 by performing combined time-reversal and parity transformations, and therefore gives rise to the same positive angular displacement. Similarly, step 4 can be mapped to step 1. This is verified in the inset of fig. 4(a), where we superimpose the angular displacement at each step of the swimming stroke as a function of β. Given that for steps 2 and 3 the relative distances between the beads are smaller than for steps 1 and 4, the angular displacement tends to be larger for the former. The net displacement is therefore positive for a wide range in β. For the range $107° \lesssim \beta \lesssim 120°$ the numerics show that steps 1 and 4 dominate, causing negative net angular displacements.

Based on their sense of rotation, we can divide swimmers into three main groups. The first group, corresponding to positive $\Delta\theta$, is delimited by two vanishing points, located at $\beta = 0°$ and $\beta \approx 107°$, with a maximum located at $\beta \approx 53°$. Within the same range of angles, the translational displacement, $|\Delta\mathbf{r}|$, decreases with increasing β to a minimum located at $\beta \approx 103°$ and then increases again. For the second group of swimmers the angular displacement is negative, as shown in fig. 4(a), and also has a non-monotonic behaviour, here $\Delta\theta$ decreases for $\beta > 107°$ up to a minimum value, roughly located at $\beta = 113°$, and then increases again, vanishing at $\beta \approx 120°$. In this same range the translational displacement increases monotonically for angles larger than $103°$. For $\beta > 120°$, corresponding to the third group of swimmers, both the angular and translational displacements increase monotonically. These results are summarised in fig. 5, where we depict the reciprocal radius of the swimmer trajectory, D/R_t, as a function of the swimmer angle, β (in units of the rest link length, D). The sign of D/R_t reflects the sense of motion along the trajectory, being clockwise for $D/R_t < 0$ and anti-clockwise if $D/R_t > 0$. Angles for
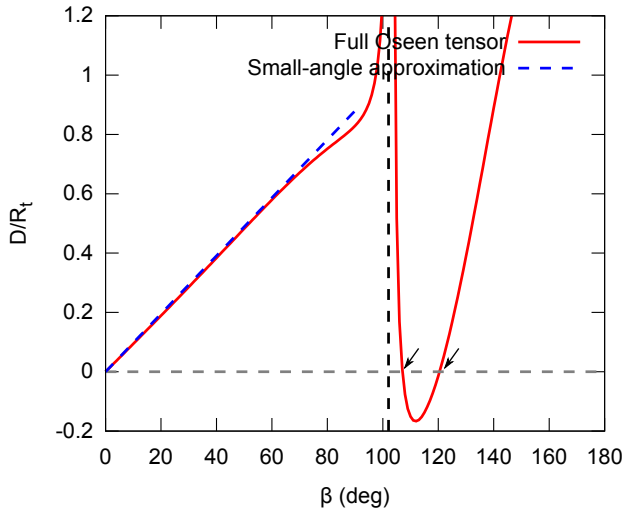
Fig. 5. Normalised curvature of the swimmer trajectory as a function of the swimmer angle, β. The solid line corresponds to the numerical solution of the Oseen-tensor hydrodynamics while the dashed curve corresponds to the perturbative result. The arrows indicate the β values for which swimmers describe a linear motion. The vertical asymptote indicates a purely rotating swimmer. Model parameters are $R/D = 10^{-1}$ and $\epsilon/D = 10^{-1}$.

which swimmers have linear trajectories, corresponding to a vanishing angular displacement in fig. 4(a), are indicated by arrows. The purely rotating swimmer, with vanishing $|\Delta \mathbf{r}|$ but finite $\Delta\theta$ is indicated by the asymptote located at $\beta \approx 103°$.

Apart from giving a useful insight into the circle swimming exhibited by the model, fig. 5 can be used as a readout to choose a particular swimmer, depending on the desired radius of trajectory and sense of motion. This can be useful given the wide range of radii that the trajectories can adopt. While the range in β that results in clockwise motion is rather narrow, one can always obtain the desired direction of motion by considering negative values of β (mirror image swimmer).

4 Velocity fields

Based on the qualitative change in the trajectory with the swimmer angle, we expect that the flow field created by the swimmers also changes with β. This is interesting in terms of the hydrodynamic interactions with surrounding objects, *e.g.* passive particles, both small tracers and extended objects, and other swimmers. The average velocity field is calculated as

$$\bar{\mathbf{v}}_i = \frac{1}{T} \int_0^T \sum_j \mathbf{H}_{ij} \cdot \mathbf{F}_j \, \mathrm{d}t, \qquad (15)$$

where i denotes a point in space with position vector $\mathbf{r}_i$ in the frame of reference of the hydrodynamic centre of the swimmer with the links oriented at an angle $\beta/2$ with respect to the x-axis.

Figures 6 and 7 depict the direction (arrows) and magnitude (colours) of $\bar{\mathbf{v}}_i$ for $\beta = \{0°, 53°, 107°\}$ and $\beta = \{113°, 120°, 140°\}$, respectively. We plot the velocity field at two different length scales: on the left we show the range $-2D < x, y < 2D$, and on the right we show the range $-20D < x, y < 20D$. At small length scales the strength of the velocity field is higher close to beads 1 and 3, and is weakly dependent on β. The flow pattern resembles that of the linear swimmer for small β, for $\beta > 107°$ the swimmers exhibit a recirculation pattern, up to distances comparable to the swimmers body length. This behaviour, however, is rapidly lost at larger length scales, as shown in the left panels of figs. 6 and 7.

We consider now the far-field behaviour. Quadrupolar decays (a velocity field which scales with distance as r^{-3}) arise generally for swimmers whose stroke is invariant under a combined time-reversal and parity transformation [37]. This invariance must be reflected in the velocity field —resulting in odd-power decays. For our swimmer the symmetry holds when the extension and deformation of both legs are identical. While the flow patterns for $\beta > 0$ are in general reminiscent of a stresslet velocity field, a closer inspection of the magnitude of the velocity shows that it does indeed have a power law decrease with distance governed by an exponent $n = -3$. Figure 8(a) plots the apparent decay exponent, n, measured at a large distance from the swimmer, as a function of β. We consider the decay along the the x- and y-axes, and define n as

$$n(y=0) = \left. \frac{\partial \ln |\mathbf{v}_i|}{\partial \ln x} \right|_{y=0} \qquad (16)$$

and

$$n(x=0) = \left. \frac{\partial \ln |\mathbf{v}_i|}{\partial \ln y} \right|_{x=0}. \qquad (17)$$

Since the exponent is measured at a finite distance from the swimmer, its value is in general non-integer. However, for sufficiently long measuring distances we expect to recover a single integer value for n. Along the y-axis the apparent exponent is always closer to $n = -3$, indicating that the quadrupolar term in the velocity field dominates at long distances as expected. This holds along the x-axis as well, except for $\beta \approx \{83°, 126°\}$, where higher-order terms in the expansion dominate the decay, as indicated by the larger exponent $n < -4$. This behaviour is interesting, as it suggests that the symmetry of the swimmer at these angles suppresses the contribution of the quadrupolar term and gives way to higher order terms in the multipole expansion.

In order to demonstrate the change in the behaviour of the far-field velocity as the swimmer loses its invariance under a time-reveral and partity transformation, we have measured the apparent exponent for asymmetric swimmers, where l_1 and l_2 have maximum extensions $0.8D$ and D, while all other parameters are kept as before. The results, presented in fig. 8(b), show apparent exponents along the x- and y-axes, which are consistent with a dipolar decay ($n = -2$).
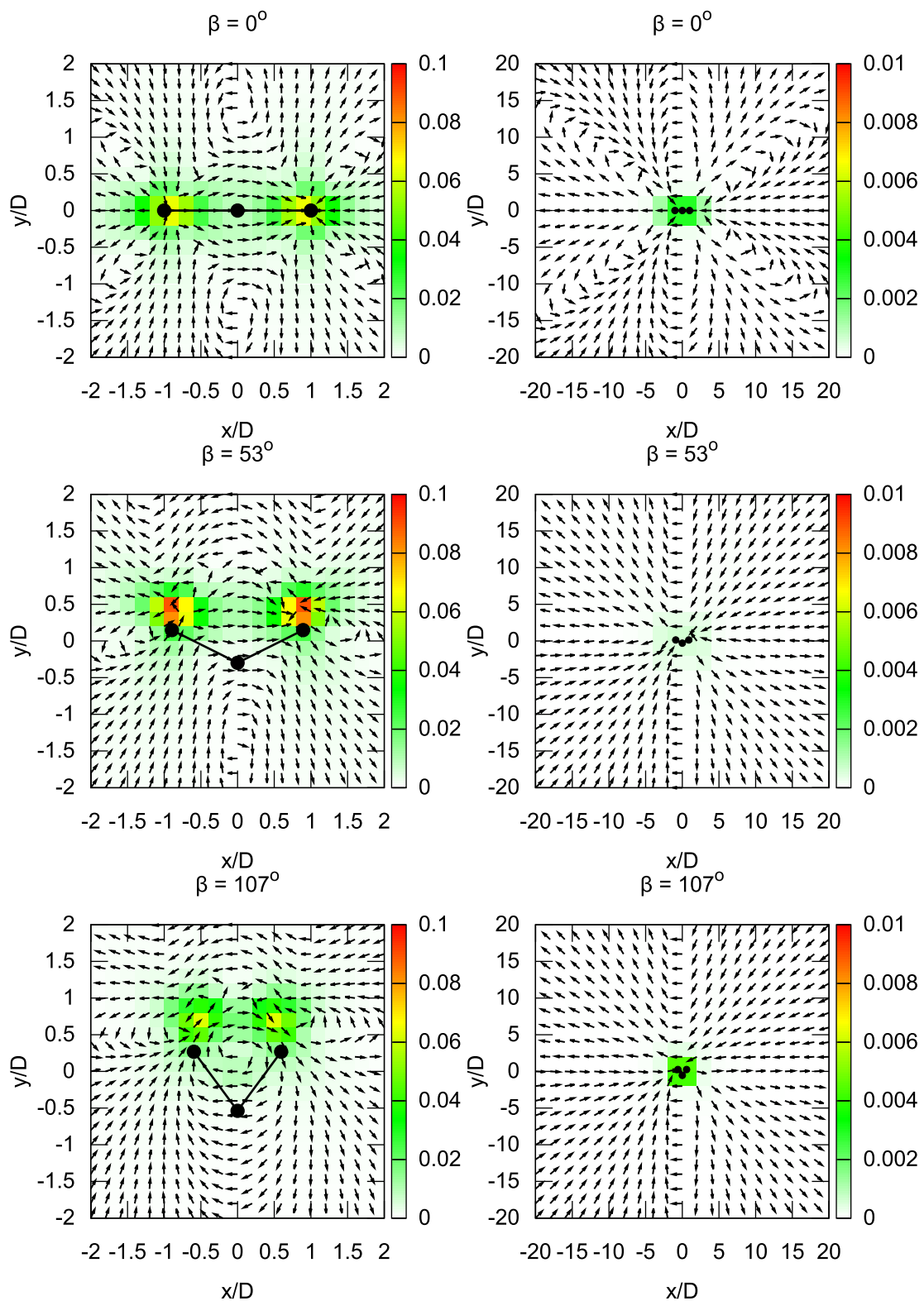
Fig. 6. (Colour on-line) Average velocity fields near (left) and far (right) from the swimmer for $\beta = 0°$, 53°, and 107°. Arrows indicate the direction of the velocity field, $\mathbf{v}_i/|\mathbf{v}_i|$, while the colour scale indicates its normalised magnitude, $P|\mathbf{v}_i|/\epsilon$.
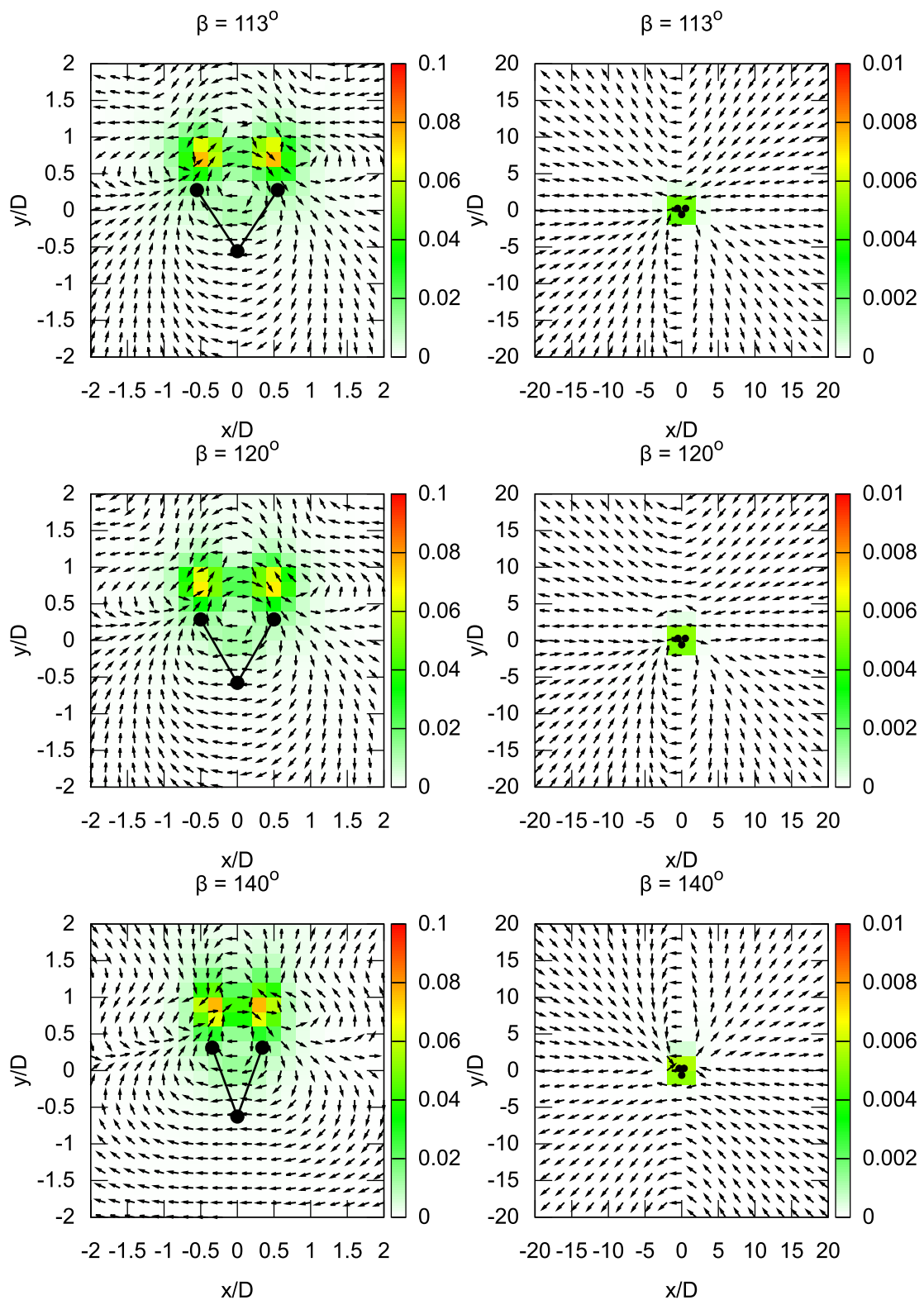
Fig. 7. Average velocity fields near (left) and far (right) from the swimmer for $\beta = 113°$, $120°$, and $140°$. Arrows indicate the direction of the velocity field, $\mathbf{v}_i/|\mathbf{v}_i|$, while the colour scale indicates its normalised magnitude, $P|\mathbf{v}_i|/\epsilon$.
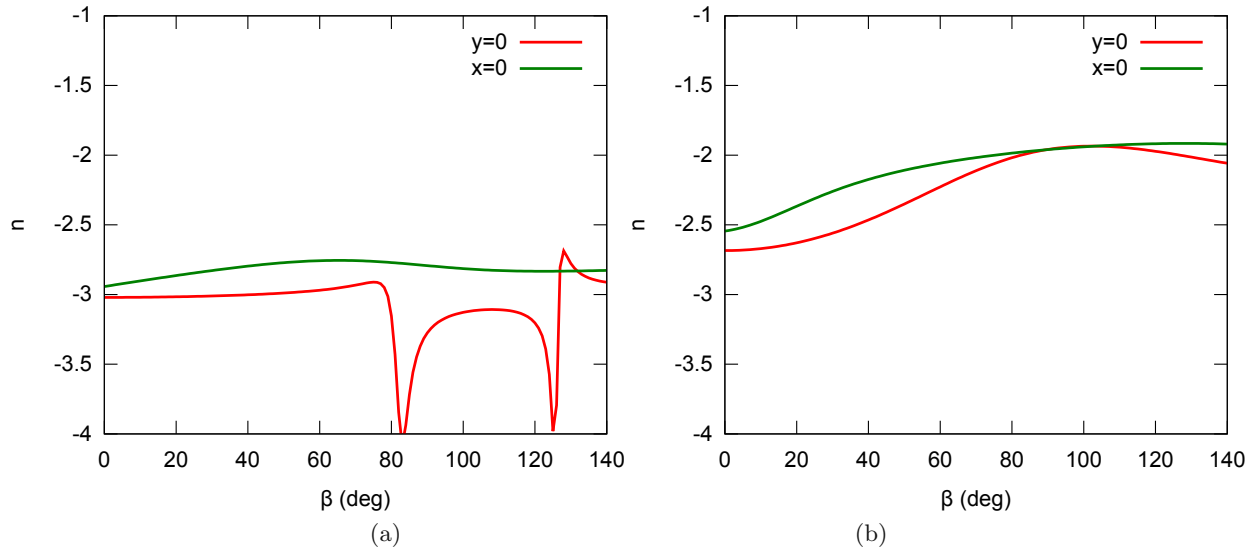
Fig. 8. Apparent exponent governing the decay of the magnitude of the velocity field along the x- and $y-$axes with distance, as a function of the swimmer angle β. (a) Symmetric swimmer with identical maximum arm extension, D. (b) Asymmetric swimmer with maximum arm extensions $0.8D$ and D, for l_1 and l_2.
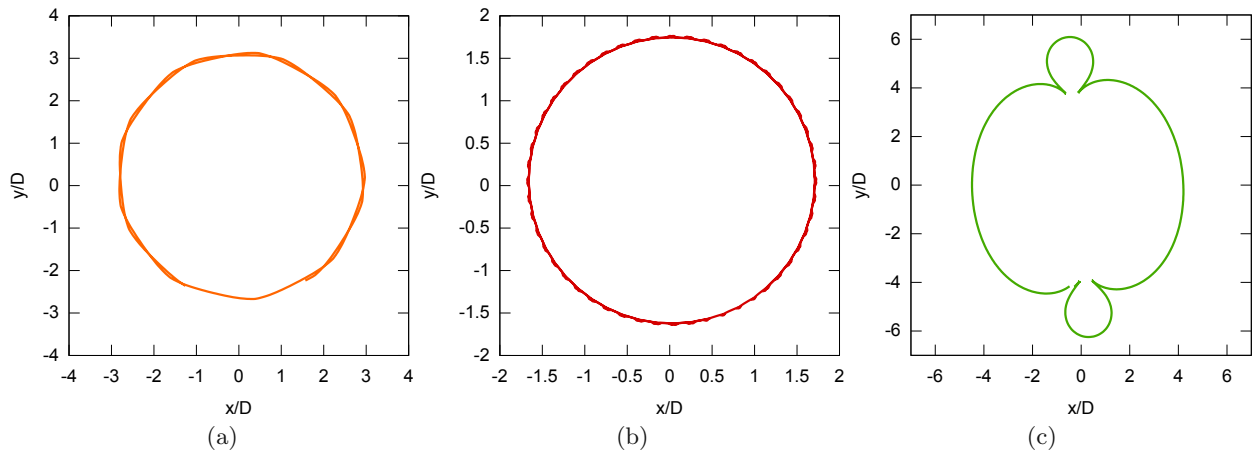

Fig. 9. Example of swimming pattern where the swimmer angle of the swimmer varies according to $\beta(t) = \beta_0 + \hat{\beta}\sin(\Omega t)$, with (a) $\beta_0 = 53°$, $\hat{\beta} = \beta_0/2$ and $\Omega = 2\pi/1000P$, (b) $\beta_0 = 80°$, $\hat{\beta} = \beta_0/2$, and $\Omega = 2\pi/1000P$ and (c) $\beta_0 = 80°$, $\hat{\beta} = 4\beta_0/5$ and $\Omega = 2\pi/50000P$.

5 Conclusions

In this paper we have proposed a simple three-sphere model for a circle swimmer which is a natural generalisation of the linear Najafi-Golestanian swimmer [5]. The spheres are placed on a triangle such that two subsequent strokes are performed at an angle. We find that the radius and the sense of rotation of the swimmer trajectory depend delicately on the separation angle between the rods joining the beads. The velocity field produced by this simple circle swimmer exhibits a characteristic inverse-power decay at large distances. For swimming strokes invariant under a combined time-reversal and parity transformation we recover the expected quadrupolar decay for the velocity field, except for a narrow range of separation angles where a stronger decay is observed. As expected, for asymmetric swimming strokes, which do not posses the time-reversal

and parity symmetry, we recover a decay consistent with a dipolar velocity field.

The model can serve as a simple reference to help understand more complex situations such as a circle swimmer in a confining geometry or the collective properties of many circle swimmers. A further extension of the model is to swimmers whose angle varies in time [7,8]. Here we expect that more complicated modes of motion arise, depending on the interplay between the timescale of the link variation and the timescale of the swimmer angle variation. Since the latter essentially controls the radius of the swimming trajectory, a slow variation of the swimmer angle relative to the links results in more complex swimming patterns, as shown in fig. 9, where the trajectories have a varying curvature leading to meandering motion. Any arbitrary two-dimensional trajectory can be generated by a suitable choice of $\beta(t)$. Hence $\beta(t)$ can be used

as a "steering wheel" to navigate at will. Similar ideas, related to the controllability of the swimmer trajectories, have been recently explored by Alouges *et al.* [43]. The motion of circle swimmers under shear (*e.g.*, linear shear or Poiseuille flow) can lead to new trajectories such as cycloids. Other external driving that could alter trajectories include a gravitational field or magnetic or electric fields [44]. One is just beginning to understand the topologies of these trajectories for simple noise-free circle swimmers [38].

The trajectories of the circle swimmers studied in this paper could also be verified experimentally, *e.g.*, by controlling the trajectories of immersed microbeads using optical traps, as performed by Leoni *et al.* [45] for the linear three-bead swimmer, and there is no obstacle in principle to do this for our circle swimmer as well.

Finally, putting together more than three spherical beads could lead to more complicated motion, in three dimensions, than the simple circular trajectories discussed in this paper. This results from the intricate translation-rotation coupling for biaxial particles. It was shown that the simple Brownian circle swimmer in three spatial dimensions possesses a wealth of different trajectories with the circular helix being the simplest one [46]. It would be interesting to generalise our model to four spheres which are not in a common plane in order to access these complicated types of motion.

References

1. J. Toner, Y.H. Tu, S. Ramaswamy, Ann. Phys. **318**, 170 (2005).
2. P. Hänggi, F. Marchesoni, Rev. Mod. Phys. **81**, 387 (2009).
3. M.E. Cates, Rep. Prog. Phys. **75**, 042601 (2012).
4. P. Romanczuk, M. Bär, W. Ebeling, B. Lindner, L. Schimansky-Geier, Eur. Phys. J. ST **202**, 1 (2012).
5. A. Najafi, R. Golestanian, Phys. Rev. E **69**, 062901 (2004).
6. J.E. Avron *et al.*, New J. Phys. **7**, 234 (2005).
7. R. Dreyfus, J. Baudry, H.A. Stone, Eur. Phys. J. B **47**, 161 (2005).
8. D.J. Earl, C.M. Pooley, J.F. Ryder, I. Bredberg, J.M. Yeomans, J. Chem. Phys. **126**, 064703 (2007).
9. R. Golestanian, A. Ajdari, Phys. Rev. E **77**, 036308 (2008).
10. R. Golestanian, Eur. Phys. J. E **25**, 1 (2008).
11. G.P. Alexander, J.M. Yeomans, Europhys. Lett. **83**, 34006 (2008).
12. E. Lauga, D. Bartolo, Phys. Rev. E **78**, 030901 (2008).
13. A.M. Leshansky *et al.*, New J. Phys. **9**, 145 (2009).
14. G.J. Elfring, E. Lauga, Phys. Rev. Lett. **103**, 088101 (2009).
15. H.C. Berg, L. Turner, Biophys. J. **58**, 919 (1990).
16. W.R. DiLuzio, L. Turner, M. Mayer, P. Garstecki, D.B. Weibel, H.C. Berg, G.M. Whitesides, Nature **435**, 1271 (2005).
17. E. Lauga, W.R. DiLuzio, G.M. Whitesides, H.A. Stone, Biophys. J. **90**, 400 (2006).
18. J. Hill, O. Kalkanci, J.L. McMurry, H. Koser, Phys. Rev. Lett. **98**, 068101 (2007).
19. V.B. Shenoy, D.T. Tambe, A. Prasad, J.A. Theriot, Proc. Natl. Acad. Sci. U.S.A. **104**, 8229 (2007).
20. S. Schmidt, J. van der Gucht, P.M. Biesheuvel, R. Weinkamer, E. Helfer, A. Fery, Eur. Biophys. J. **37**, 1361 (2008).
21. I.H. Riedel, K. Kruse, J. Howard, Science **309**, 300 (2005).
22. D.M. Woolley, Reproduction **126**, 259 (2003).
23. B.M. Friedrich, F. Jülicher, New J. Phys. **10**, 123025 (2008).
24. S. Nakata, Y. Iguchi, S. Ose, M. Kuboyama, T. Ishii, K. Yoshikawa, Langmuir **13**, 4454 (1997).
25. G. Volpe, I. Buttinoni, D. Vogt, H.J. Kümmerer, C. Bechinger, Soft Matter **7**, 8810 (2011).
26. B. ten Hagen, Bachelor thesis, University of Düsseldorf (2011).
27. H.C. Crenshaw, Amer. Zool. **36**, 608 (1996).
28. E.M. Purcell, Am. J. Phys. **45**, 3 (1977).
29. J. Dunstan, G. Mino, E. Clement, R. Soto, Phys. Fluids **24**, 011901 (2012).
30. H. Shum, E.A. Gaffney, D.J. Smith, Proc. R. Soc. London, Ser. A **466**, 1725 (2010).
31. M. Leoni, T.B. Liverpool, EPL **92**, 64004 (2010).
32. Y. Fily, A. Baskaran, M.C. Marchetti, Soft Matter **8**, 3002 (2012).
33. S. van Teeffelen, H. Löwen, Phys. Rev. E **78**, 020101 (2008).
34. S. van Teeffelen, U. Zimmermann, H. Löwen, Soft Matter **5**, 4510 (2009).
35. B. ten Hagen, S. van Teeffelen, H. Löwen, J. Phys.: Condens. Matter **23**, 194119 (2011).
36. C.M. Pooley, G.P. Alexander, J.M. Yeomans, Phys. Rev. Lett. **99**, 228103 (2007).
37. G.P. Alexander, C.M. Pooley, J.M. Yeomans, Phys. Rev. E **78**, 045302 (2008).
38. B. ten Hagen, R. Wittkowski, H. Löwen, Phys. Rev. E **84**, 031105 (2011).
39. J. Dunkel, V.B. Putz, I.M. Zaid, J.M. Yeomans, Soft Matter **6**, 4268 (2010).
40. V.B. Putz, J.M. Yeomans, J. Stat. Phys. **137**, 1001 (2009).
41. G.J. Elfring, E. Lauga, Phys. Fluids **23**, 011902 (2011).
42. R. Golestanian, J.M. Yeomans, N. Uchida, Soft Matter **7**, 3074 (2011).
43. F. Alouges, A. Desimone, L. Heltai, A. Lefebvre-Lepot, B. Merlet, arxiv:1007.4920v2.
44. H. Löwen, J. Phys.: Condens. Matter **13**, R415 (2001).
45. M. Leoni, J. Kotar, B. Bassetti, P. Cicuta, M. Cosentino Lagomarsino, Soft Matter **5**, 472 (2008).
46. R. Wittkowski, H. Löwen, Phys. Rev. E **85**, 021406 (2012).